PHYSICAL REVIEW B VOLUME 25, NUMBER 2 15 JANUARY 1982

Complex band structures of zinc-blende materials

Yia-Chung Chang
Department of Physics and Materials Research Laboratory, University of Illinois at Urbana-Champaign, Urbana, Illinois 61801
(Received 26 May 1981)

A theoretical method is presented for calculating the complex band structures of a solid. Using this method, we have studied the evanescent Bloch functions associated with 14 zinc-blende materials for various crystallographic orientations and directions, and have obtained new insight into the topological structure of the complex bands in solids. The present application of the general method is based on a 10-band nearest-neighbor tight-binding model which is capable of producing realistic band structures for most semiconductors and insulators. The method is conceptually simple and computationally efficient. The evanescent Bloch solutions obtained with the present model can be used to study various electronic properties associated with solid surfaces, interfaces, and superlattices.

I. INTRODUCTION

During the past decade, there has been a great increase of interest in solid surfaces and interfaces. Many theoretical techniques have been developed to treat these problems.[1–4] In a pioneering paper,[5] Heine has pointed out that an electronic wave function near a solid surface (or interface) may be obtained by matching the allowed solutions on the two sides of a boundary plane. To match at every point of the boundary plane, one needs to know all the solutions of the Schrödinger equation in the crystal at a given energy E,[5,6] including those associated with complex values of the wave vector k_z normal to the surface—the evanescent states. The relationship between the energy E and the evanescent states is contained in the so-called complex band structure.

Several calculations of complex band structures for metals and semiconductors have been previously performed[7–11] with techniques requiring rather heavy computation for realistic models. In this paper we present a simple and computationally fast method for calculating the complex band structures and evanescent states for solids. This method is based on a realistic nearest-neighbor tight-binding model in which five atomic orbitals (sp^3 plus an excited s-like orbital) for each lattice site are used. Hjalmarson *et al.*[12–14] have shown that with appropriately chosen parameters this model provides a good representation of the valence bands as well as the lowest conduction band of almost all zinc-blende materials. Since our method is conceptually simple and computationally efficient, while taking into account the important features of the solid, it has immediate application to problems such as solid surfaces, interfaces, and superlattices.

We studied the complex band structures of 14 zinc-blende materials including C, Si, Ge, α-Sn, GaAs, GaP, GaSb, AlAs, AlP, InAs, InP, InSb, ZnSe, and ZnTe for the (100), (111), and (110) orientations. For each orientation, the wave vector parallel to the corresponding surface $\bar{k}$ is kept real and the wave vector normal to the surface k_z is allowed to be complex. Here and henceforth, we shall use $\vec{k}$ to denote the three-dimensional wave vector and $\bar{k}$ to denote the projection of $\vec{k}$ on the plane parallel to the surface. We find that for the (100) and (111) orientations with $\bar{k} = 0$, the complex band structures can be obtained through analytic procedures. For other cases the complex band structures are obtained through simple numerical procedures, which involve finding the roots of a polynomial of order ten or less.

In Sec. II we discuss the basic problem of finding the complex band structure of solids and some simple mathematical tricks which can be employed to simplify the problem. In Sec. III we discuss the method used to obtain the evanescent Bloch states of the bulk material for the (100), (111), and (110) orientations. We show that the complex wave vectors k_z associated with these evanescent states can be obtained by finding the zeros of a finite-order polynomial and that the coefficients of the polyno-

mial can be obtained easily. In Sec. IV we present the results for the complex band structures of six typical zinc-blende materials and various orientations. We discuss the topology of these three-dimensional band structures and its relation to the symmetry properties of the crystal. In Sec. V a summary and some concluding remarks are presented.

II. BASIC PROBLEM

The conventional method of obtaining the band structures of solids is to find the eigenvalues of the Hamiltonian $H(\vec{k})$ as functions of the real wave vector $\vec{k}$, i.e., to solve the Schrödinger equation

$$H(\vec{k})\psi=E(\vec{k})\psi. \tag{1}$$

In this calculation we are interested in the real energy solutions to Eq. (1) for complex wave vectors $\vec{k}$. In general one can diagonalize the Hamiltonian matrix $H(\vec{k})$ for each fixed complex value of $\vec{k}$ and select out the resulting real energy eigenvalues. This procedure is useful for special cases (e.g., $\bar{k}=0$) where the real energy solutions are known (by symmetry considerations) to exist along some special paths (e.g., the imaginary axis) in the complex k_z plane. Schulman and McGill[10] have used this procedure to study the complex band structures of metals and semiconductors along the special directions. For general cases this procedure has difficulty in finding the correct paths (the so-called real lines) on which the real energy solution lies.

The alternative is to find the solution k_z to Eq. (1) for each fixed real values of E and $\bar{k}$. Equivalently, one finds the zeros of the determinant function

$$d(k_z)\equiv\det[H(\bar{k},k_z)-E1_0], \tag{2}$$

where 1_0 is an identity matrix. In a tight-binding (TB) approximation, the determinant $d(k_z)$ is in general a polynomial in the variable $\xi\equiv e^{ik_za'}$, where a' is the distance between two adjacent layers parallel to a given surface, i.e.,

$$d(k_z)=\sum_{\sigma=-N/2}^{N/2}h^{(\sigma)}e^{i\sigma k_za'}, \tag{3}$$

where N is the order of the polynomial, which equals $2m$ (m being the number of neighbors included in the TB approximation) times the number of independent atomic orbitals on an atomic plane parallel to the surface.[11] To find these coefficients $h^{(\sigma)}$, we first evaluate the determinant $d(k_z)$ using Eq. (2) for $(N+1)$ arbitrary trial values of k_z (denoted as k_λ; $\lambda=1,\ldots,N+1$), we then obtain a matrix equation

$$\sum_{\sigma=1}^{N+1}T_{\sigma\lambda}h^{(\sigma-1-N/2)}=d(k_\lambda), \tag{4a}$$

where

$$T_{\sigma\lambda}\equiv e^{i(\sigma-1-N/2)k_\lambda a'}. \tag{4b}$$

The coefficients $h^{(\sigma)}$ can be obtained by multiplying T^{-1} on both sides of Eq. (4a) and the complex k_z solutions are simply the roots of the polynomial given in Eq. (3).

For zinc-blende materials, the TB Hamiltonian matrix $H(\vec{k})$ as a function of the wave vector $\vec{k}$ can be written in the block form

$$H(\vec{k})=\begin{bmatrix}A & V(\vec{k})\\ V'(\vec{k}) & C\end{bmatrix}, \tag{5}$$

where A, C, $V(\vec{k})$, and $V'(\vec{k})$ represent the anion-anion, cation-cation, anion-cation, and cation-anion interaction matrices, respectively. In the nearest-neighbor tight-binding model with five atomic orbitals per site,[12–14] the off-diagonal elements of the matrices A and C all vanish and the diagonal elements are given by the on-site atomic energies:

$$A_{ii}=\epsilon_a^{\bar{s}},\epsilon_a^{s},\epsilon_a^{p},\epsilon_a^{p},\epsilon_a^{p}$$

and

$$C_{ii}=\epsilon_c^{\bar{s}},\epsilon_c^{s}\epsilon_c^{p},\epsilon_c^{p},\epsilon_c^{p},\quad i=1,\ldots,5.$$

The anion-cation interaction matrix is given by

$$V_{ij}(\vec{k})=P_{ij}g_{n_{ij}}(\vec{k}), \tag{6}$$

where p_{ij} and n_{ij} are elements of the 5×5 matrices P and n defined by

$$P=\begin{bmatrix}0 & 0 & V_{\bar{s}_0p} & V_{\bar{s}_0p} & V_{\bar{s}_0p}\\ 0 & V_{ss} & V_{s_0p} & V_{s_0p} & V_{s_0p'}\\ -V_{\bar{s}_1p} & -V_{s_1p} & V_{xx} & V_{xy} & V_{xy}\\ -V_{\bar{s}_1p} & -V_{s_1p} & V_{xy} & V_{xx} & V_{xy}\\ -V_{\bar{s}_1p} & -V_{s_1p} & V_{xy} & V_{xy} & V_{xx}\end{bmatrix} \tag{7a}$$

and

$$n=\begin{bmatrix}0&0&1&2&3\\0&0&1&2&3\\1&1&0&3&2\\2&2&3&0&1\\3&3&2&1&0\end{bmatrix}. \tag{7b}$$

The cation-anion matrix $V'(\vec{k})$ is related to $V(\vec{k})$ by

$$V'_{ij}(\vec{k})=V_{ji}(-\vec{k}). \tag{8}$$

It should be noted that for real $\vec{k}$, $V'(\vec{k})=V^{+}(\vec{k})$, the Hermitian conjugate of $V(\vec{k})$. In Eqs. (6)–(8) we have written the nearest-neighbor interactions in terms of the product of a $\vec{k}$-independent matrix P_{ij} (which contains all the nearest-neighbor parameters) and a parameter-independent matrix $g_{n_{ij}}(\vec{k})$. The functions $g_n(\vec{k})$; $n=0, 1, 2, 3$ are defined in Ref. 15. We find that they can be expressed in a compact, symmetric form as

$$\begin{aligned}g_n=\tfrac{1}{4}(&e^{i(k_1+k_2+k_3)a/4}+e^{i(k_1-k_2-k_3)a/4}\epsilon_{2n}\epsilon_{3n}\\&+e^{i(-k_1+k_2-k_3)a/4}\epsilon_{1n}\epsilon_{3n}\\&+e^{i(-k_1-k_2+k_3)a/4}\epsilon_{1n}\epsilon_{2n}),\end{aligned} \tag{9}$$

where

$$\epsilon_{nn'}\equiv\begin{cases}+1 \text{ for } n=n'\\-1 \text{ for } n\neq n'\end{cases}, \tag{10}$$

and a is the lattice constant. This tight-binding model includes 13 empirical parameters, i.e., $\epsilon_a^{\bar{s}}$, ϵ_a^s, ϵ_a^p, $\epsilon_c^{\bar{s}}$, ϵ_c^s, ϵ_c^p, $V_{\bar{s}_0p}$, V_{s_0p}, $V_{\bar{s}_1p}$ V_{s_1p}, V_{ss}, V_{xx}, and V_{xy}. Those parameters which yield a good fit to the band structures of 14 zinc-blende semiconductors can be found in Refs. 13 and 14. Combining Eq. (1) with (5), we write

$$\begin{bmatrix}A-E1_0 & V(\vec{k})\\ V'(\vec{k}) & C-E1_0\end{bmatrix}\begin{bmatrix}\psi_a\\ \psi_c\end{bmatrix}=0, \tag{11}$$

where ψ_a and ψ_c are five-dimensional column vectors, denoting the anion and cation components of ψ, respectively, 1_0 denotes an identity matrix of dimension five. For energy E not equal to $\epsilon_a^{\bar{s}}$, ϵ_a^s, or ϵ_a^p, we may substitute the equation

$$\psi_a=-(A-E1_0)^{-1}V(\vec{k})\psi_c \tag{12}$$

into Eq. (11) and obtain

$$\begin{bmatrix}A-E1_0 & V(\vec{k})\\ 0 & D(\vec{k})\end{bmatrix}\begin{bmatrix}\psi_a\\ \psi_c\end{bmatrix}=0, \tag{13}$$

where

$$\begin{aligned}D(\vec{k})\equiv&-V'(\vec{k})(A-E1_0)^{-1}V(\vec{k})\\&+C-E1_0.\end{aligned} \tag{14}$$

Since A and C are diagonal, Eq. (14) can be written more explicitly as

$$\begin{aligned}D_{ij}(\vec{k})=&-\sum_k P_{ki}P_{kj}g_{n_{ki}}(-\vec{k})g_{n_{kj}}(\vec{k})/a_k\\&+c_i\delta_{ij},\end{aligned} \tag{15}$$

where

$$a_k\equiv A_{kk}-E,$$

and

$$c_i\equiv C_{ii}-E.$$

In Eq. (15) we used the relations (6) and (8). Comparing Eq. (13) with (2), we find

$$d(k_z)=\left[\prod_{i=1}^{5}a_i\right]\det[D(\vec{k})]. \tag{16}$$

It should be noted that Eq. (16) holds true for arbitrary values of E, since according to Eq. (2), $d(k_z)$ is also a polynomial in E and the factor $(\prod_{i=1}^{5}a_i)$ should cancel all the poles of $\det[D(\vec{k})]$ in Eq. (16). We have thus far reduced the problem to that of finding the zeros of a five-dimensional determinant function $d(k_z)$. In Sec. III we discuss how to find the evanescent Bloch states for various faces.

III. EVANESCENT STATES FOR (100), (111), AND (110) FACES

To find the evanescent states associated with a given surface, we first specify the energy E and the wave vector parallel to the surface $\bar{k}$. Only real values of $\bar{k}$ are of interest, since the Hamiltonian is invariant under the translation parallel to the surface or interface of concern. As mentioned in Sec. II, the complex wave vectors k_z associated with the evanescent states are simply the zeros of the determinant function $d(k_z)$, which is a finite polynomial in $e^{ik_za'}$ and $e^{-ik_za'}$, a' being the distance between two adjacent layers. The procedure of obtaining the evanescent states will be discussed below for the (100), (111), and (110) faces, separately.

A. (100) face

It is noted from Eq. (9) that we can write the functions $g_n(\vec{k})$ as the sum of two terms, proportional to $e^{ik_z a'/2}$ and $e^{ik_z a'/2}$, respectively, with $a' \equiv a/2$ being the distance between two adjacent layers parallel to the (100) plane, viz.,

$$g_n(\vec{k}) = \tfrac{1}{4}[f_n^{(+)}(\bar{k})e^{ik_z a'/2} + f_n^{(-)}(\bar{k})e^{-ik_z a'/2}], \tag{17}$$

where

$$f_n^{(+)}(\bar{k}) \equiv e^{i(k_1+k_2)a'/2} + \epsilon_{1n}\epsilon_{2n}e^{-i(k_1+k_2)a'/2} \tag{18a}$$

and

$$f_n^{(-)}(\bar{k}) \equiv e^{i(k_1-k_2)a'/2}\epsilon_{2n}\epsilon_{3n} + e^{-i(k_1-k_2)a'/2}\epsilon_{1n}\epsilon_{3n}. \tag{18b}$$

From Eq. (6) it is obvious that the nearest-neighbor interaction matrix $V(\vec{k})$ can also be written as the sum of two terms proportional to $e^{ik_z a'/2}$ and $e^{-ik_z a'/2}$, respectively. Physically these two terms represent the couplings of a given atomic plane to the adjacent plane on the right and left sides, respectively. Substituting Eqs. (17) and (15) into (16), one can show that the function $d(k_z)$ can be written in the polynomial form as in Eq. (3) with $N = 10$.

The problem can be further simplified by exploiting the symmetry properties of the crystal. The zinc-blende crystal has a mirror plane parallel to the (100) face. As a result the coefficients $h^{(\sigma)}(\vec{k})$ are all real. Furthermore, since the Hamiltonian is Hermitian for real k_z, we have

$$h^{(-\sigma)}(\bar{k}) = h^{(\sigma)*}(\bar{k}). \tag{19}$$

Therefore, Eq. (3) can be rewritten as

$$d(k_z) = \sum_{n=0}^{5} C_n(\bar{k})\xi^n, \tag{20}$$

where $\xi \equiv \cos(k_z a/2)$ and C_n are related to $\{h^{(\sigma)}\}$ by a simple transformation.

For the special case $\bar{k} = 0$, the complex band structure can be obtained analytically. It is noted that when $\bar{k} = 0$, $g_2 = g_3 = 0$ and the Hamiltonian $H(\vec{k})$ is immediately decomposed into 4×4 and 6×6 matrices. Following the reduction procedure discussed in Sec. II, one can show that the determinant function $d(k_z)$ can be written as the product of a quadratic and a cubic polynomial for the variable $\xi \equiv \cos(k_z a/2)$. The two roots of the quadratic polynomial are degenerate and can be expressed as

$$\xi = 2[(\epsilon_a^p - E)(\epsilon_c^p - E) - V_{xy}^2]/(V_{xx}^2 - V_{xy}^2) - 1. \tag{21}$$

The roots of the cubic polynomial are somewhat lengthy to write down, but can be handled analytically without difficulty.[16]

B. (111) face

For the (111) face, we define a new coordinate system in which the wave vectors $\bar{k}$ [parallel to the (111) plane] and k_z [normal to the (111) plane] are given by

$$k_z = \frac{1}{\sqrt{3}}(k_1+k_2+k_3),$$
$$\bar{k}_1 = (k_1+k_2-2k_3)/\sqrt{6}, \tag{22}$$
$$\bar{k}_2 = (k_1-k_2)/\sqrt{2},$$

where (k_1, k_2, k_3) is the wave vector defined in the original coordinate system. In the new coordinates we write the functions $g_n(\vec{k})$ as the sum as a term proportional to $e^{3ik_z a'/4}$ and a term proportional to $e^{-ik_z a'/4}$, where $a' \equiv a/\sqrt{3}$ is the distance between two adjacent atomic layers parallel to the (111) plane, viz.,

$$g_n(\vec{k}) = \tfrac{1}{4}[f_n^{(+)}(\bar{k})e^{3ik_z a'/4} + f_n^{(-)}(\bar{k})e^{-ik_z a'/4}], \tag{23}$$

where

$$f_n^{(+)}(\bar{k}) \equiv 1 \tag{24a}$$

and

$$f^{(-)}(\bar{k}) \equiv e^{i(\sqrt{2/3}\bar{k}_1+\sqrt{2}\bar{k}_2)a/4}\epsilon_{2n}\epsilon_{3n} + e^{i(\sqrt{2/3}\bar{k}_1-\sqrt{2}\bar{k}_2)a/4}\epsilon_{1n}\epsilon_{3n} + e^{-i\sqrt{2/3}\bar{k}_1 a/2}\epsilon_{1n}\epsilon_{2n}. \tag{24b}$$

In similarity to the (100) face, the coefficients $f_n^{(\pm)}(\bar{k})$, when multiplied by the matrix elements P_{ij} for the nearest-neighbor interaction parameters, represent the couplings of a given plane with the adjacent atomic plane located on the right and left sides, respectively. Here we have assumed that the atomic plane on the right side is more distant than

that on the left side. Substituting Eqs. (23) and (15) into (16), we obtain a polynomial equation as in (3) with $N = 10$. The coefficients $h^{(\sigma)}(\bar{k})$ in Eq. (3) for the current case are no longer real numbers, because of the lack of reflection symmetry for the (111) face, unless $\bar{k} = 0$. However, Eq. (19) remains valid and (3) can be rewritten as

$$d(k_z)=\sum_{n=0}^{5} C_n\xi^n+\eta\sum_{n=0}^{4} C_{n+6}\xi^n=0, \tag{25}$$

where C_n, $n=0,\ldots,10$ are real coefficients, related to the real and imaginary parts of $h^{(\sigma)}$, $\sigma=0,\ldots,5$, $\xi\equiv\cos(k_z a/\sqrt{3})$, and $\eta\equiv\sin\times(k_z a/\sqrt{3})$. Equation (25) can be transformed into a 10th order polynomial equation for the variable ξ, since $\eta = \pm(1-\xi^2)^{1/2}$.

As for the (100) face, the $\bar{k} = 0$ case for the (111) face is analytic. From Eq. (23) it is noted that $g_1 = g_2 = g_3$, when $\bar{k} = 0$, and the Hamiltonian $H(\bar{k})$ can be block diagonalized by a unitary transformation in which the x,y,z orbitals are transformed into the ω,u,v orbitals defined by

$$\omega\equiv\frac{1}{\sqrt{3}}(x+y+z),$$

$$u\equiv\frac{1}{\sqrt{2}}(x-y),$$

$$v\equiv\frac{1}{\sqrt{6}}(x+y-2z).$$

The transformed Hamiltonian is decomposed into a 4×4 matrix and a 6×6 matrix. Using the same reduction procedure described above, we can write $d(k_z)$ as the product of a quadratic and a cubic polynomial for the variable $\xi\equiv\cos(k_z a/2\sqrt{3})$. The two roots of the quadratic polynomial are degenerate and are given by

$$\xi=\frac{2[4(\epsilon_a^p-E)(\epsilon_c^p-E)-(V_{xx}+V_{xy})^2]}{[(V_{xx}-V_{xy})(3V_{xx}+V_{xy})]}-1. \tag{26}$$

The analytic expressions for the roots of the cubic polynomial are somewhat lengthy and, hence, are not presented here.

C. (110) face

For the (110) face, a convenient coordinate system is chosen such that the wave vectors $\bar{k}$ and $\bar{k}_z$, which are parallel and normal to the (110) plane, respectively, are given by

$$\begin{aligned}\bar{k}_1&=k_3,\\ \bar{k}_2&=(k_1-k_2)/\sqrt{2},\\ k_z&=(k_1+k_2)/\sqrt{2},\end{aligned} \tag{27}$$

where $(k_1 k_2,k_3)$ is the wave vector in the original coordinate system. The g functions written in the new coordinates are

$$g_n(\vec{k})=\tfrac{1}{4}[e^{i\bar{k}_1 a/4}(e^{ik_z a'}+\epsilon_{1n}\epsilon_{2n}e^{-ik_z a'})+f_n(\bar{k})], \tag{28}$$

where

$$f_n(\bar{k})\equiv e^{-i\bar{k}_1 a/4}(\epsilon_{2n}e^{i\bar{k}_2 a'}+\epsilon_{1n}e^{-i\bar{k}_2 a'})\epsilon_{3n}, \tag{29}$$

and $a'\equiv a/2\sqrt{2}$ is just the distance between two adjacent layers parallel to the (110) plane. Unlike the previous cases, the g functions for the (110) face each contains three terms, the first two being proportional to $e^{ik_z a'}$ and $e^{-ik_z a'}$, respectively, and the third being independent of k_z. This is not surprising. The (110) plane contains both cations and anions, whereas the (100) or (111) plane contains either cations or anions. The first two terms in Eq. (28) couple a given atomic (110) plane with an adjacent one on the right and left sides, respectively. The third term simply represents the intralayer coupling between cations and anions.

Substituting Eqs. (28) and (15) into (16), we then obtain a polynomial expression for the function $d(k_z)$ as in Eq. (3) with $N = 20$. Because the reflection symmetry is preserved for the (110) face, all the coefficients, $h^{(\sigma)}(\bar{k})$ are real numbers. Using the property that $h^{(-\sigma)}(\bar{k})=h^{(\sigma)}(\bar{k})$ [from Eq. (19)], we rewrite Eq. (3) as

$$d(k_z)=\sum_{n=0}^{10} C_n\xi^n, \tag{30}$$

where $\xi\equiv\cos(k_z a/2\sqrt{2})$.

For the special case $\bar{k} = 0$, the Hamiltonian matrix $H(\vec{k})$ can be decoupled into 2×2 and 8×8 matrices. This is easily seen by transforming the x and y basis orbitals into the u_+ and u_- orbitals defined by $u_\pm\equiv(1/\sqrt{2})(x\pm y)$. The determinant function $d(k_z)$ can therefore be written as the product of a quadratic and 8th-order polynomial for the variable ξ. The two roots of the quadratic polynomial are given by

$$\xi_{\pm}=\frac{\{\pm 2[(\epsilon_a^p-E)(\epsilon_c^p-E)]^{1/2}-V_{xy}-V_{xx}\}}{(V_{xx}-V_{xy})}. \tag{31}$$

The expression (31) will be used later to examine the analytic properties of the associated complex band structures.

The polynomial $d(k_z)$ in Eq. (3) has been reduced to various forms given by Eqs. (20), (25), and (30) for the (100), (111), and (110) faces, respectively. Instead of using Eq. (4) to obtain the coefficients $h^{(\sigma)}$ and transforming them into C_n in Eqs. (20), (25), and (30), we find it more convenient to obtain C_n directly from the relation

$$\sum_{n=0}^{M-1} T'_{\mu n} C_n = d_\mu, \tag{32}$$

where d_μ are the determinants evaluated using Eq. (16) at M trial points k_μ, $M = 6$, 11, and 11 for the (100), (111), and (110) faces, respectively. $T'_{\mu n} = \cos^n(k_\mu a')$ for the (100) and (110) faces and

$$T'_{\mu n}=\begin{cases}\cos^n(k_\mu a') & \text{if } n \le 5\\ \sin(k_\mu a')\cos^{n-6}(k_\mu a') & \text{if } n \ge 6\end{cases} \tag{33}$$

for the (111) face. The coefficients C_n are obtained by multiplying $(T')^{-1}$ on both sides of Eq. (32) and the polynomial equations (20), (25), and (30) are solved numerically for various faces.

IV. RESULTS AND DISCUSSIONS

We studied the complex band structures of the 14 zinc-blende materials including C, Si, Ge, α-Sn, GaAs, GaP, GaSb, AlAs, AlP, InAs, InP, InSb, ZnSe, and ZnTe for the (100), (111), and (110) faces. The results for the $\bar{k} = 0$ case for some typical materials: Si, Ge, α-Sn, GaAs, InP, and ZnTe are plotted in Figs. 1—6 for the [100] direction, in Figs. 7—12 for the [111] direction, and in Figs. 13—18 for the [110] direction. The complex band structures for the other materials are found to have similar topological features. For example, C is similar to Si, InAs, InSb, and ZnSe are similar to InP, and the rest are similar to GaAs.

We classify these complex band structures into four categories, namely, (1) real bands ($\mathrm{Im}k_z = 0$), (2) imaginary bands of the first kind ($\mathrm{Im}k_z \neq 0$ and $\mathrm{Re}k_z = 0$), (3) imaginary bands of the second kind ($\mathrm{Im}k_z \neq 0$ and $\mathrm{Re}k_z = k_{\max}$, where $k_{\max}$ is $2\pi/a$, $\sqrt{3}\pi/a$, and $2\sqrt{2}\pi/a$ for the [100], [111], and

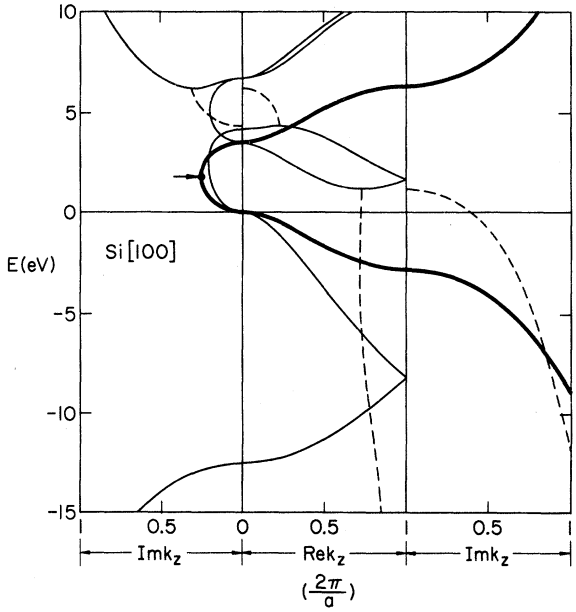

FIG. 1. Complex band structure of Si along [100] direction. Real bands (solid curves), imaginary bands of the first and second kinds (solid curves) are plotted in the middle, left, and right panels, respectively. The real portion of complex bands (broken curves) is plotted in the middle panel, and the associated imaginary portion (broken curves) is plotted in the left or right panels, depending on whether the end points are closer to the origin or boundary of the Brillouin zone.

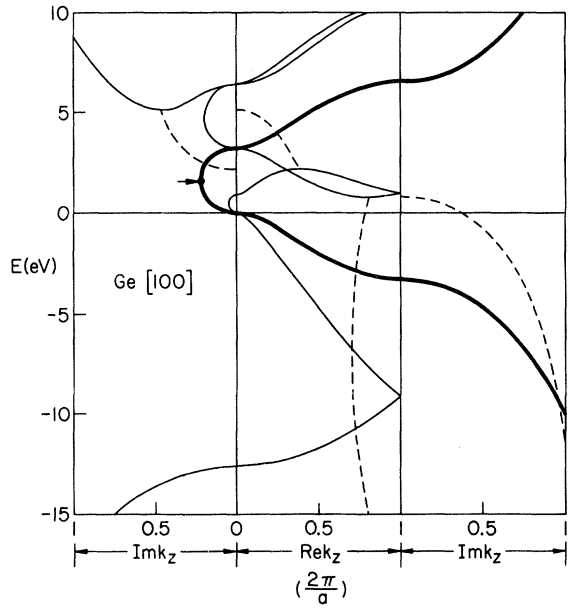

FIG. 2. Complex band structure of Ge along [100] direction. The notation is the same as in Fig. 1.

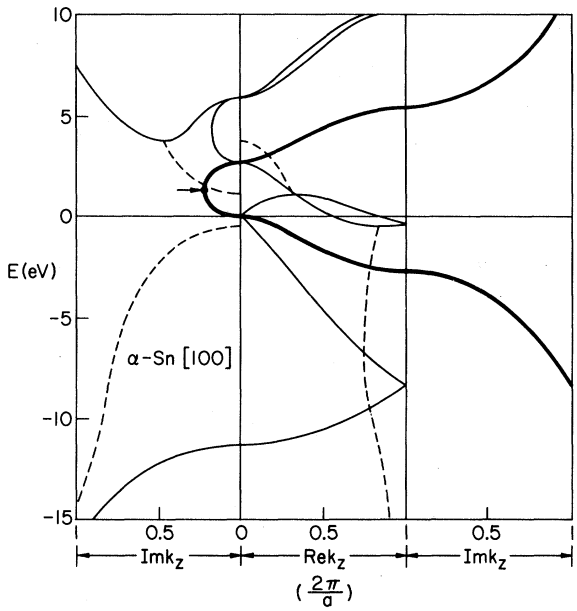

FIG. 3. Complex band structure of α-Sn along [100] direction. The notation is the same as in Fig. 1.

[110] directions, respectively), and (4) complex bands (Re$k_z \neq 0$ or $k_{\max}$ and Im$k_z \neq 0$). In Figs. 1–18, the imaginary bands of the first kind, the real bands and the imaginary bands of the second kind are plotted in the left, middle, and right panels (solid lines), respectively. The complex bands are denoted by pairs of broken lines, with their real portion plotted in the middle panel and their imaginary portion plotted in the left or right panels, depending on whether the complex bands are connected to imaginary bands of the first or second kinds.

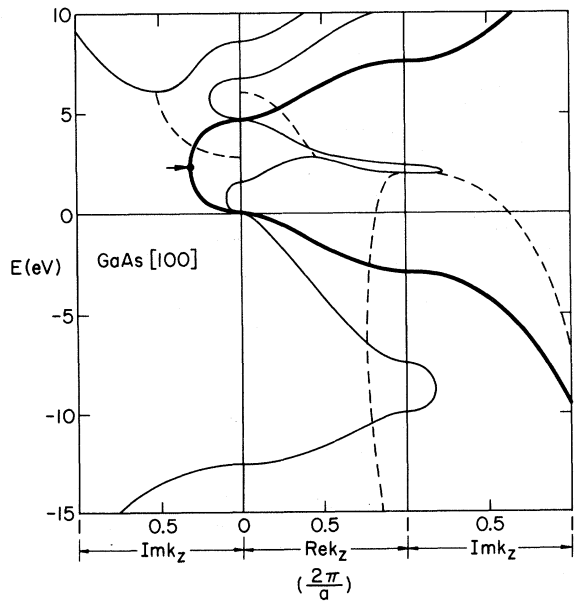

FIG. 4. Complex band structure of GaAs along [100] direction. The notation is the same as in Fig. 1.

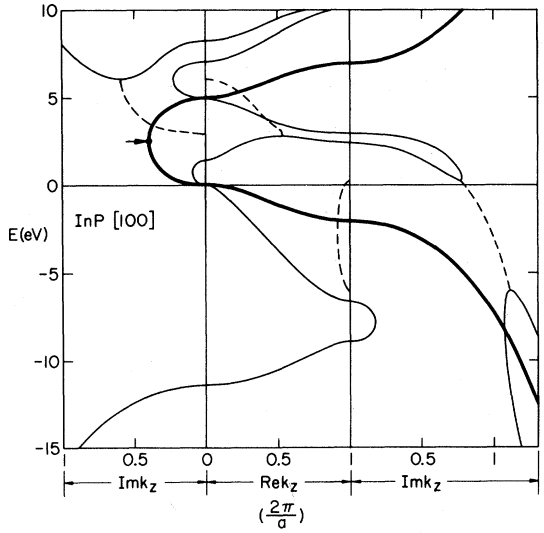

FIG. 5. Complex band structure of InP along [100] direction. The notation is the same as in Fig. 1.

It should be noted that if k_z is a solution associated with energy E, then both $-k_z^*$ and k_z^* are also solutions associated with E, i.e.,

$$E(-k_z^*)=E(k_z)=E(k_z^*), \tag{34}$$

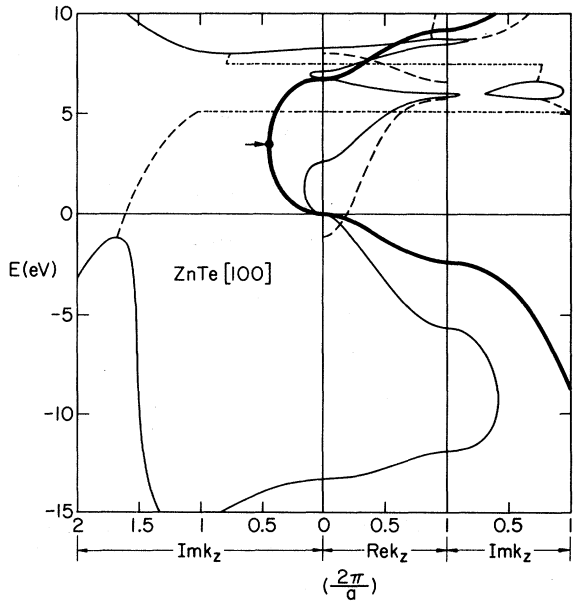

FIG. 6. Complex band structure of ZnTe along [100] direction. The notation is the same as in Fig. 1.

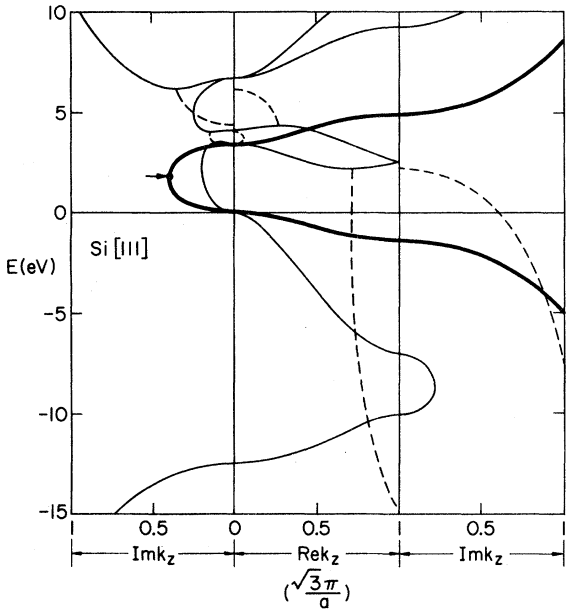

FIG. 7. Complex band structure of Si along [111] direction. The notation is the same as in Fig. 1.

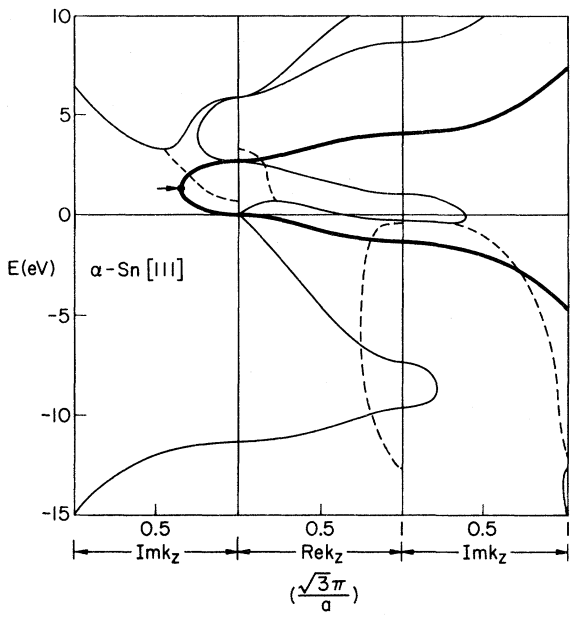

FIG. 9. Complex band structure of α-Sn along [111] direction. The notation is the same as in Fig. 1.

where k_z^* denotes the complex conjugate of k_z. The first equality in Eq. (34) is the direct result of time-reversal symmetry[17,18] [which states that $E(-\vec{k}^*) = E(\vec{k})$] and the requirement $\vec{k} = 0$. The second equality is due to the fact that $H^+(\vec{k}) = H(\vec{k}^*)$ which implies $E^*(\vec{k}) = E(\vec{k}^*)$.[18] In Figs. 1—18, only the absolute values of Rek_z and Imk_z are plotted. The actual solutions can be inferred according to Eq. (34).

We may consider the complex band structure as a collection of N continuous complex functions of E [$k_\lambda(E)$, $\lambda = 1, \ldots, N$] where $N = 10$, 10, and 20 for the (100), (111), and (110) faces, respectively. These functions when traced in the complex k_z

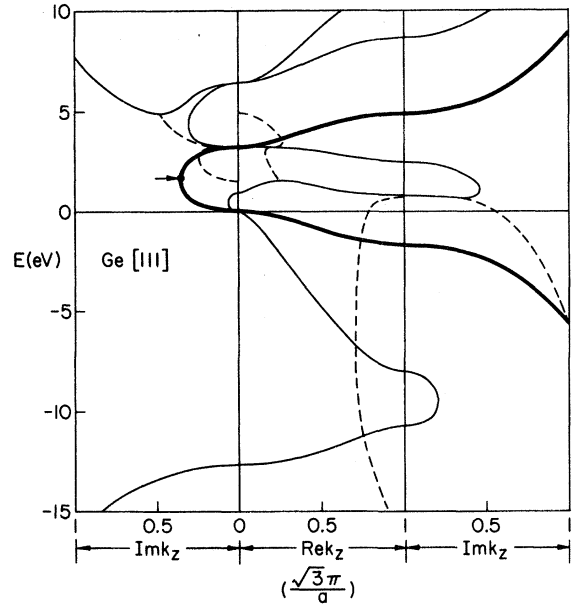

FIG. 8. Complex band structure of Ge along [111] direction. The notation is the same as in Fig. 1.

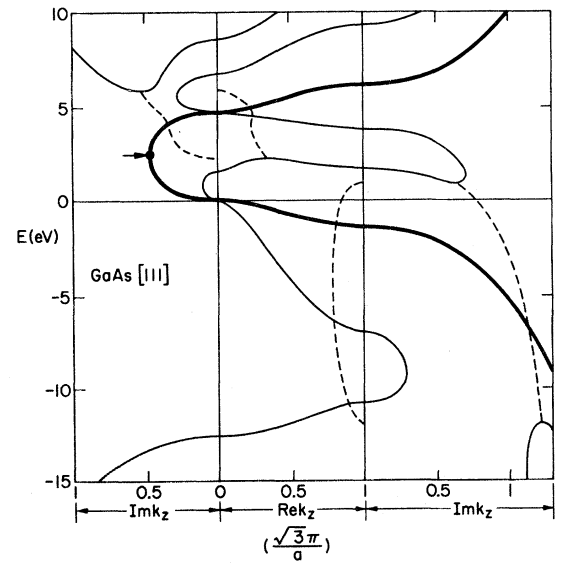

FIG. 10. Complex band structure of GaAs along [111] direction. The notation is the same as in Fig. 1.

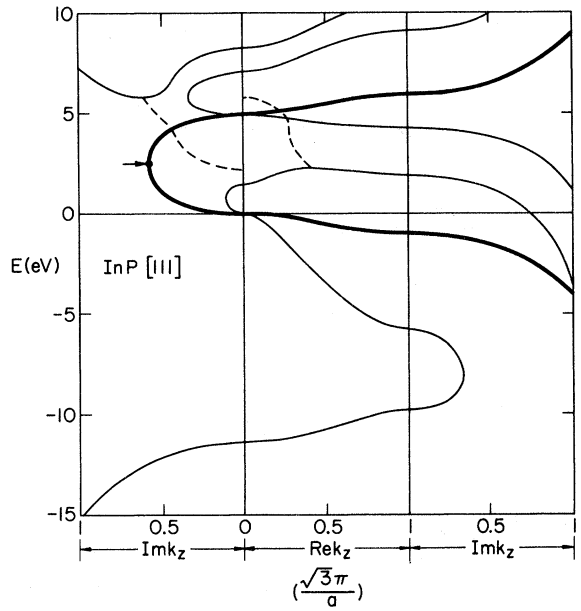

FIG. 11. Complex band structure of InP along [111] direction. The notation is the same as in Fig. 1.

plane, as energy varies from $-\infty$ to ∞, are hereafter referred to as real lines. Heine[5] has examined the general features of the complex band structures for three-dimensional systems and proposed several rules for the real lines. These rules are summarized below.

(i) The real lines cannot terminate or branch. Conversely no two or more real lines can coalesce into one.

(ii) Two real lines can in general cross each other, but this is vanishingly possible except where k_z is real. At the crossing point the energy E must be an extremum when plotted along the real axis.

(iii) A real line can loop back to the real k_z axis, but only if it encloses at least one branch

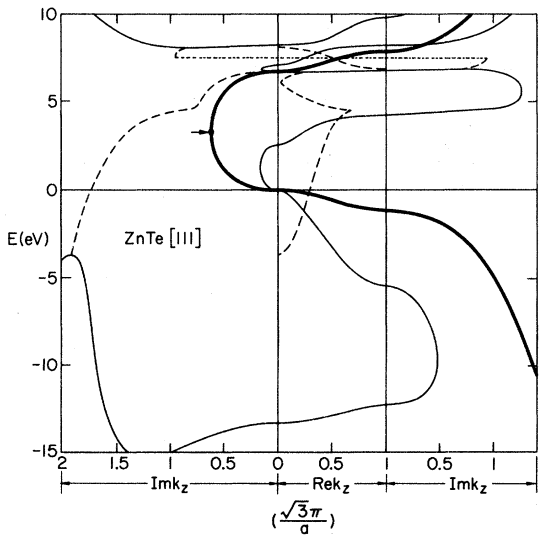

FIG. 12. Complex band structure of ZnTe along [111] direction. The notation is the same as in Fig. 1.

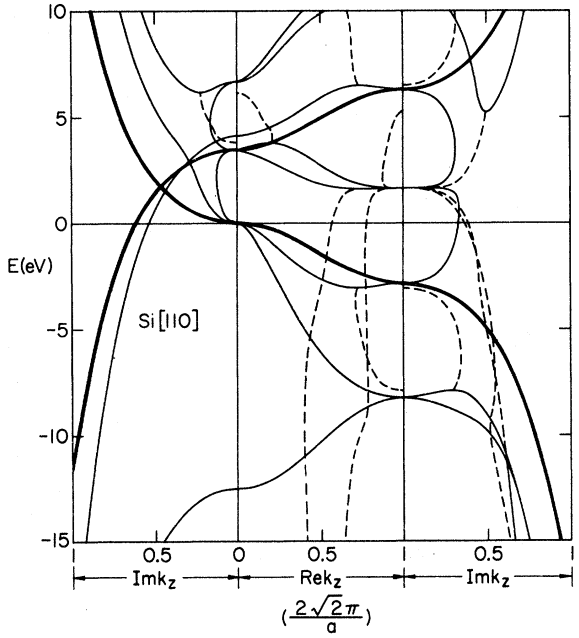

FIG. 13. Complex band structure of Si along [110] direction. The notation is the same as in Fig. 1.

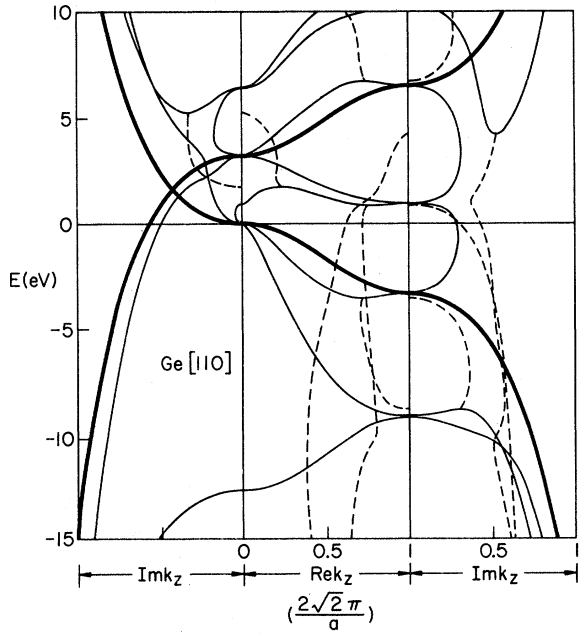

FIG. 14. Complex band structure of Ge along [110] direction. The notation is the same as in Fig. 1.

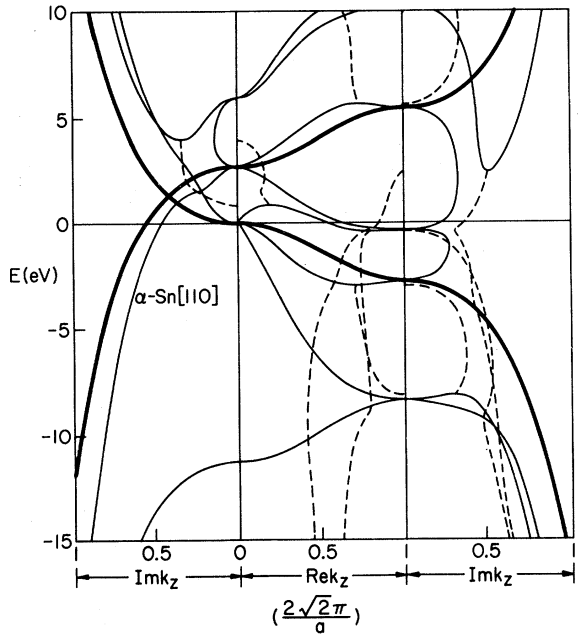

FIG. 15. Complex band structure of α-Sn along [110] direction. The notation is the same as in Fig. 1.

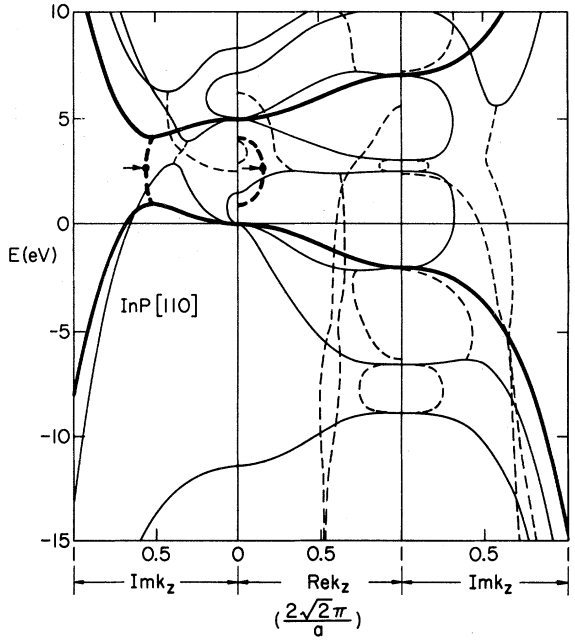

FIG. 17. Complex band structure of InP along [110] direction. The notation is the same as in Fig. 1.

point in the complex k_z plane.

All these rules apply to our complex band structures with one exception. In Figs. 1—18 several real lines are found to cross each other at complex k_z points with $\mathrm{Im}k_z \neq 0$ and $\mathrm{Re}k_z = 0$ or $k_{\max}$. At these points the energy E has an extremum when plotted along the corresponding imaginary axes. According to Heine,[5] it is vanishingly possible for $E(k_z)$ to be real and dE/dk_z to be zero at the same point in the sense of Herring,[19] unless k_z is on the real axis where the first requirement is automatically satisfied. However, if the complex band structure has the reflection symmetry, i.e., $E(-k_z) = E(k_z)$, then it can be shown that[5,18]

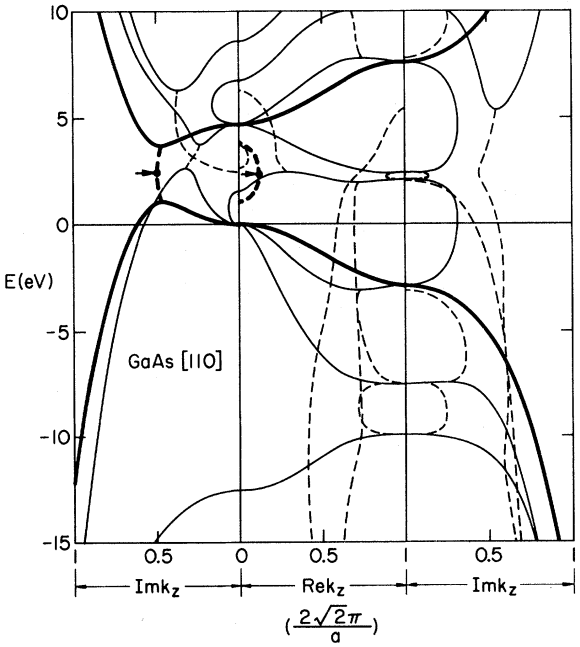

FIG. 16. Complex band structure of GaAs along [110] direction. The notation is the same as in Fig. 1.

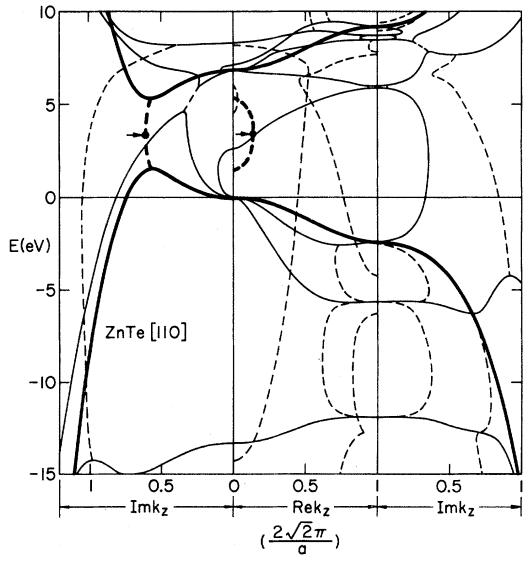

FIG. 18. Complex band structure of ZnTe along [110] direction. The notation is the same as in Fig. 1.

$$E(k_z)=[E(k_z)]^* \tag{35}$$

for $\mathrm{Re}k_z=\frac{1}{2}g_{001}$, where g_{001} is a reciprocal-lattice vector in the z direction. Consequently it is no longer vanishingly possible for $E(k_z)$ to have an extremum at a complex k_z point with $\mathrm{Re}k_z=\frac{1}{2}g_{001}$ (i.e., $\mathrm{Re}k_z=0$ or $k_{\max}$ in the present case).

We now discuss the detailed features of the complex band structures shown in Figs. 1—18. Note that the left panels of Figs. 1—12 all contain five distinct imaginary bands of the first kind. The middle three bands are closed loops when plotted in the E-$\mathrm{Im}k_z$ plane (including the portion with $\mathrm{Im}k_z<0$), with their maxima and minima connected to real bands of the same symmetry. The highest imaginary band has a minimum at certain nonzero values of $\mathrm{Im}k_z$ and runs to infinity as E goes to infinity. The bands indicated by thick lines are doubly degenerate and are obtained by using the analytic expressions Eqs. (21) and (26) for the (100) and (111) faces, respectively. To illustrate the analytic properties of the bands, we rewrite Eqs. (21) and (26) in the form

$$E=\frac{\epsilon_a^p+\epsilon_c^p}{2}\pm\left[\left[\frac{\epsilon_a^p-\epsilon_c^p}{2}\right]^2+c\cos^2(k_za')+b\right]^{1/2}, \tag{36}$$

where for the [100] direction, $a'\equiv a/2$, $b\equiv V_{xy}^2$, and $c\equiv V_{xx}^2-V_{xy}^2$ and for the [111] direction, $a'\equiv a/2\sqrt{3}$, $b\equiv(V_{xx}+V_{xy})^2/4$, and $c\equiv(V_{xx}-V_{xy})(3V_{xx}+V_{xy})/4$. From Eq. (36), it is apparent that a branch point occurs when $E=(\epsilon_a^p+\epsilon_c^p)/2$. This is indicated by an arrow in Figs. 1—12.

The middle panels of Figs. 1—12 contain mainly the real bands. For all materials except ZnTe, it is found that the conduction bands (with Δ_2' symmetry and Λ_3 symmetry for the [100] and [111] directions, respectively) have a maximum at k_z somewhere in the middle of the Brillouin zone. This maximum and the minimum of the highest imaginary band mentioned above are always connected by a complex band (indicated by broken lines).

The major features of the right portions of Figs. 1—12 include (1) two doubly degenerate imaginary bands of the second kind running to infinity as energy E goes to $-\infty$ or ∞. (2) A conjugate pair of complex bands running to infinity as E goes to $-\infty$ and (3) closed-loop imaginary bands of the second kind connecting the real bands at the X or L point whenever there is a gap. The conjugate pair of complex bands are either connected to the minimum of the (real) conduction band (e.g., Si[100]) or the minimum of the closed-loop imaginary band (e.g., InP[100] and GaAs[111]).

It is found that the complex band structure for ZnTe in the current model is conspicuously different from those for the other materials. In particular, the complex band structure of ZnTe has a special feature in which an imaginary band of the first kind is connected to an imaginary band of the second kind by a complex loop whose real part sweeps across the whole Brillouin zone (see Figs. 6 and 12). The part of the complex loop connected to the imaginary band of the first kind is plotted in the left panel and the other part plotted in the right panel of Figs. 6 and 12. The thin dashed lines in these figures indicate the connection of these two parts. Another special feature of Figs. 6 and 12 is the existence of a closed-loop imaginary band of the second kind which connects up two complex bands.[20,21] The complex band structure for Si[111] also has a special feature in which two imaginary bands of the first kind are connected by a complex loop. This feature is also found in a previous calculation using a pseudopotential method.[8]

The complex band structures shown in Figs. 13—18 are considerably more complicated than those shown in Figs. 1—12. This is due to the fact

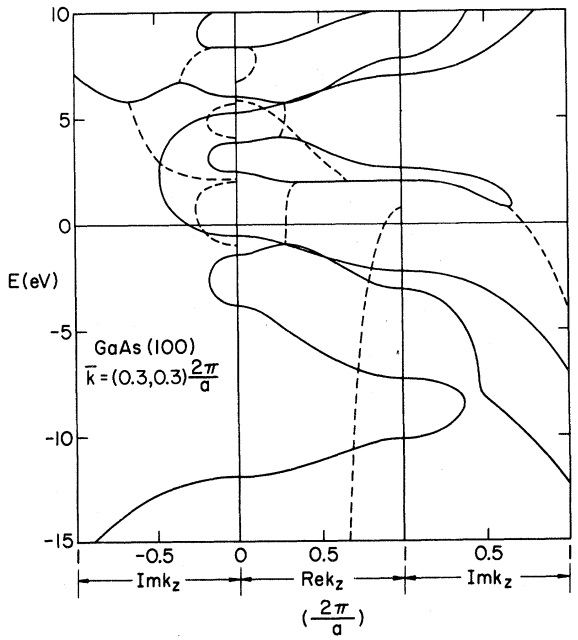

FIG. 19. Complex band structure of GaAs for (100) face with $\bar{k}=(0.3,0.3)2\pi/a$. The notation is the same as in Fig. 1.

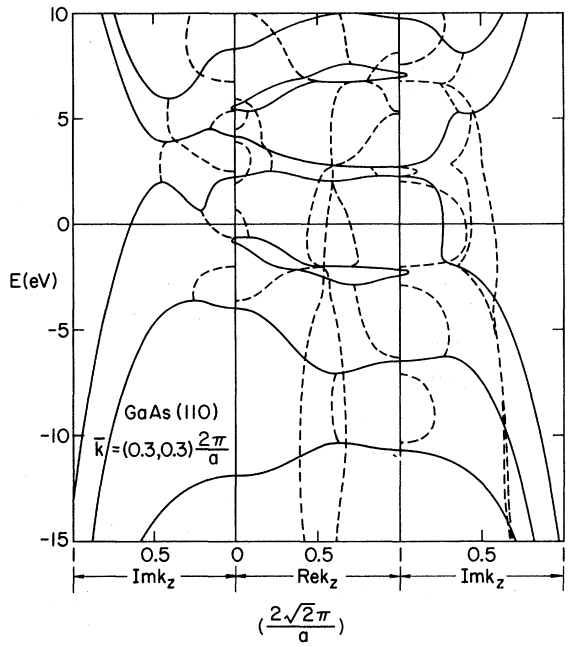

FIG. 20. Complex band structure of GaAs for (110) face with $\bar{k} = (0.3,0.3)2\pi/a$. The notation is the same as in Fig. 1.

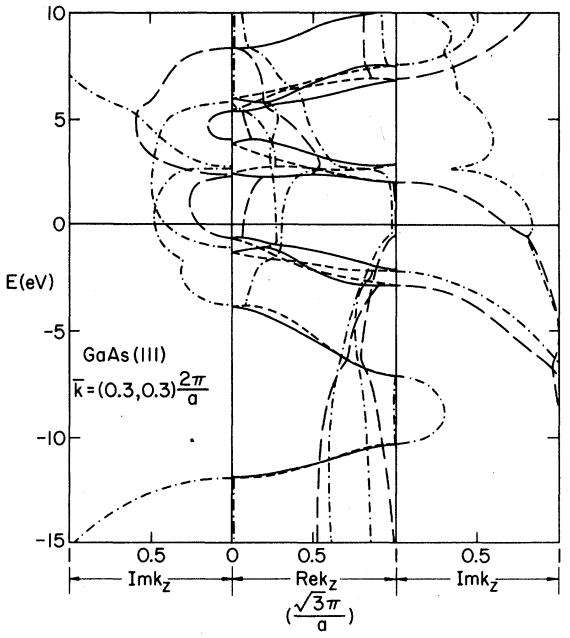

FIG. 21. Complex band structure of GaAs for (111) face with $\bar{k} = (0.3,0.3)2\pi/a$. The solid and short dashed lines in the middle panel indicate real bands with positive and negative values of k_z, respectively. The pairs of long dashed lines and dash-dot-dash lines indicate complex bands with positive and negative values of Rek_z, respectively.

that the (110) face contains both anions and cations, thus giving rise to twice as many complex k_z solutions for each energy E as there were for the (100) and (111) faces. The bands indicated by thick lines in Figs. 13–18 are obtained using Eq. (31). The analytic property of these bands can be readily understood by rewriting Eq. (31) in the form

$$E=\frac{\epsilon_a^p+\epsilon_c^p}{2}\pm[(b_+\xi+b_-)^2+\Delta^2]^{1/2}, \qquad (37)$$

where $b_\pm \equiv (V_{xx} \mp V_{xy})/2$ and $\Delta \equiv (\epsilon_a^p - \epsilon_c^p)/2$. It is noted that the function $E(k_z)$ has two branch points at $\xi = -(b_- \pm i\Delta)/b_+$, except when $\Delta = 0$ (true for covalent materials). This conjugate pair of complex branch points is sitting on the real lines where $E = (\epsilon_a^p + \epsilon_c^p)/2$. The real and imaginary parts of the branch points are indicated by arrows in Figs. 16–18. This is a very special and interesting feature of the nearest-neighbor tight-binding model, since in general it is vanishingly probable for the energy associated with a branch point being real at a general complex k_z point.[5] The complex band structure for the [110] direction exhibits several new topological features. For example, many imaginary bands of both kinds are found to be connected together by complex bands. Furthermore, the minimum of the third valence band is always connected to the maximum of an imaginary band of the second kind, and the lowest two valence bands are always connected together

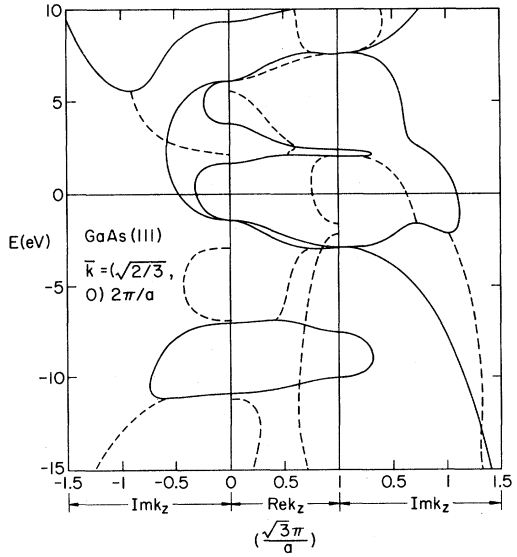

FIG. 22. Complex band structure of GaAs for (111) face with $\bar{k} = (\sqrt{2/3},0)2\pi/a$. The origin for Re$k_z$ has been shifted to $k_0 = \pi/\sqrt{3}a$ to exhibit the reflection symmetry.

by a complex band rather than an imaginary band as is the case for the [111] direction.

We have also studied the complex band structures for general cases with $\bar{k}\neq 0$. For illustration, we plot the complex band structure of GaAs for $\bar{k}=(0.3,0.3)2\pi/a$ in Figs. 19, 20, and 21 for the (100), (110), and (111) faces, respectively. The symmetry of the Hamiltonian for $\bar{k}\neq 0$ case is reduced. This lifts many degeneracies of the real bands and creates additional energy gaps at various values of k_z. Each energy gap is connected with a closed-loop imaginary band of either kind of complex band depending on whether the associated band extrema are located at $k_z = 0$, $k_{\max}$, or a general value. For the (100) and (110) faces, the reflection symmetry is preserved and the complex band structures are quite similar to those for $\bar{k} = 0$ case. The reflection symmetry no longer exists for the (111) face with a general value of $\bar{k}$. We therefore expect that k_z and $-k_z$ are in general associated with different energies. In Fig. 21, the real bands associated with negative values of k_z are denoted by dashed curves. It is also found that, because of the lack of reflection symmetry, all real band extrema no longer occur at the zone edges. Consequently, all imaginary bands of Fig. 10 turn into complex bands when $\bar{k}$ becomes nonzero. Furthermore it becomes vanishingly possible for two real lines to cross, except at real values of k_z as required by Heine's rules. All these features are illustrated in Fig. 21.

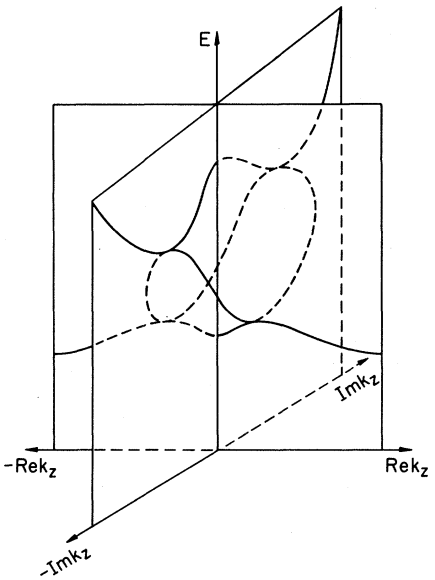

FIG. 23. Three-dimensional complex band structure illustrating the topology for an imaginary band and a real band being connected by a complex loop.

For special points in the (111) surface Brillouin zone, such as $\bar{k}=(\sqrt{2/3},0)2\pi/a$ (the $\bar{M}$ point in Ref. 21), there exists a hidden symmetry[22,23] with

$$E(\bar{k},k_0-k_z)=E(\bar{k},k_0+k_z),$$

where $k_0 = \pi/\sqrt{3a}$ or $-2\pi/\sqrt{3a}$. If we redefine the origin of the k_z as k_0, then the reflection symmetry is recovered. In Fig. 22, we plot the complex band structure of GaAs for the (111) face with $\bar{k} = (\sqrt{2/3},0)2\pi/a$. The origin of the k_z has been shifted to $k_0 = \pi/\sqrt{3a}$ to exhibit the reflection symmetry. As shown in this figure, many imaginary bands of both kinds occur and some of them have extrema at complex values of k_z with $\mathrm{Re}k_z = 0$ or $k_{\max}$ (i.e., $\mathrm{Re}k_z=\pi/\sqrt{3a}$ or $-2\pi/\sqrt{3a}$ if the origin had not been shifted).

We conclude this section by making a few remarks. The nearest-neighbor tight-binding model used to obtain these band structures is qualitatively reliable only for the valence bands and the lowest one or two conduction bands. Therefore, the complex band structures arising from the higher conduction bands should not be taken too seriously. It is, however, interesting to see what kind of topological structures this simple ten-band model can provide. It is rather gratifying that such a wealth

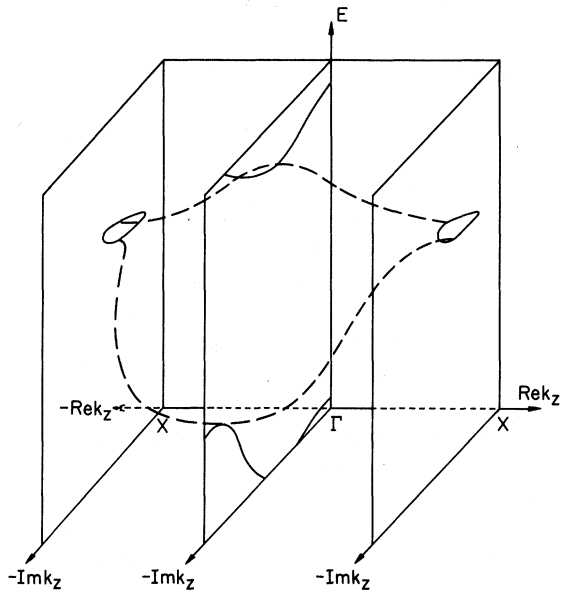

FIG. 24. Three-dimensional complex band structure illustrating the topology for an imaginary band of the first kind and an imaginary band of the second kind being connected by a complex band (dashed curve) and for two complex bands being connected by a closed-loop imaginary band of the second kind.

of information about the complex band structures can be learned from studying this simple ten-band tight-binding model. The results presented in Figs. 1—22 have provided many examples of all possible topologically distinguishable structures of the complex bands for zinc-blende semiconductors. We find several novel topological structures which have not been reported in previous studies. This is best illustrated in a three-dimensional plot, with E, $\mathrm{Re}k_z$, and $\mathrm{Im}k_z$ being the three coordinate axes. One example is shown in Fig. 23. In this figure, a complex loop (as the edge of a saddle) is connecting up one imaginary band and one real band at four complex k_z points. This is quite different from the commonly understood topology in which two real bands are connected by a complex loop at two complex k_z points. Another interesting example is shown in Fig. 24. This plot is a portion of the complex band structure shown in Fig. 6. In this figure, a pair of complex bands emanate from the maximum of an imaginary band of the first kind, then reach the minimum of an imaginary band of the second kind (the two imaginary bands of the second kind shown are equivalent since they differ by a reciprocal-lattice vector). This pair of complex bands therefore form a closed loop in the sense they begin and end at the same point. This figure also illustrates a topology in which two complex bands are connected by an imaginary band of the second kind (a closed loop).

V. SUMMARY AND APPLICATIONS

We have developed a theoretical method for calculating the complex band structures for solids. The complex $\vec{k}$ solutions to the total Hamiltonian for (100), (111), and (110) faces have been computed for 14 zinc-blende materials. This study has provided much valuable information about the hidden electronic properties associated with the bulk materials through their complex band structures. Our results exhibit a large collection of interesting topological structures for the complex bands of solids and provides some fundamental understanding of them.

The method employed to obtain these complex band structures for solids is quite simple and efficient, while maintaining the reality of the materials studied. It can be used to study the electronic properties of solid surfaces, interfaces, and superlattices. For example, one can find the surface (or interface) states by expanding the total wave function in terms of linear combinations of the propagating and evanescent Bloch states associated with a given energy in the bulk materials on both sides of the boundary plane. The expansion coefficients can be determined by matching the total wave function at the boundary plane according to appropriate boundary conditions. This calculation typically involves finding the zero of an N-dimensional determinant as a function of the energy E, where N is the number of independent tight-binding orbitals per plane times the number of surface (interface) layers which deviate from the bulk layers due to lattice relaxation. This method, therefore, has a considerable advantage over the method which involves finding the solutions for a large slab.[2,3]

Besides the large-slab approach, there also exist theoretical calculations for surfaces and interfaces using the Green's-function method.[1,4] The size of the matrix required to find the surface (or interface) states by using the Green's-function approach is comparable to that for the matching method using the evanescent states. The conventional technique for obtaining the bulk Green's function[4] involves numerical integration over k_z in the Brillouin zone for each fixed $\bar{k}$ and E. The Green's function usually has very sharp structures when plotted versus the energy E. The conventional technique cannot produce these sharp structures accurately unless a large number of mesh points for k_z is used. Allen[24,25] has realized that the integration over k_z in the bulk Green's function can be considered as a contour integral in the complex k_z plane, which can then be reduced to the sum over some finite number of complex k_z solutions to Eq. (1) (the poles of the integrand). For example, the retarded Green's function for fixed $\bar{k}$ can be written as[24,25]

$$G_0^+(\vec{r}\,\vec{r}\,';\bar{k}E)=-2\pi i\sum_\lambda \frac{\psi(\vec{r};\bar{k}k_\lambda)\psi^+(\vec{r}\,';\bar{k}k_\lambda^*)}{v_z(\bar{k}k_\lambda)}\mathrm{sgn}(z-z'), \tag{38}$$

where the k_λ's are the complex wave vectors associated with the Bloch states propagating (if k_λ is real) or decaying away (if k_λ is complex) from the plane $z=z'$,

$$v_z(\bar{k}k_\lambda)=\left.\frac{\partial E}{\partial k_z}\right|_{k_z=k_\lambda},$$

and $\psi(\vec{r};\bar{k}k_\lambda)$ is the Bloch wave function associated with the wave vector $(\bar{k},k_\lambda)$. With the technique developed in this paper, an accurate evaluation of the surface-adapted Green's function [see Eq. (38)] becomes readily feasible. From Eq. (38) it is noted[24,25] that the Green's function (and, therefore, the local density of states) has singularities at the energies E where the group velocity $v_z(\bar{k}k_\lambda)$ vanishes. This must occur at the extremum points in the complex band structure. As we mentioned previously, if the reflection symmetry exists, the complex band structure will have extrema at some complex values of k_z for which $\mathrm{Re}k_z$ is at the zone center or boundary (i.e., $\mathrm{Re}k_z = 0$ or $k_{\max}$). The topology of the complex band structures therefore plays an important role in determining the singularity structure of the Green's function with fixed $\bar{k}$.

The application of the complex band structures to problems related to solid surfaces, interfaces, and superlattices is planned to be reported in future publications.

ACKNOWLEDGMENTS

The author is indebted to many fruitful discussions with J. N. Schulman, R. E. Allen, J. D. Dow, O. F. Sankey, and G. B. Wright. The computing facility provided by the Materials Research Laboratory is gratefully acknowledged. This work is supported in part by the Office of Naval Research under Contract No. N00014-77-C-0537.

[1]J. Pollmann, in *Advances in Solid State Physics,* edited by J. Treusch (Vieweg, Braunschung, 1979), p. 117, and references therein.

[2]K. C. Pandey and J. C. Phillips, Phys. Rev. Lett. 32, 1433 (1974); 34, 1450 (1975); Phys. Rev. B 13, 750 (1976).

[3]D. J. Chadi, Phys. Rev. B 18, 1800 (1978).

[4]J. Pollmann and S. T. Pantelides, Phys. Rev. B 18, 5524 (1978), and references therein.

[5]V. Heine, Proc. Phys. Soc. London 81, 300 (1963).

[6]A. Howie, Philos. Mag. 5, 251 (1960).

[7]R. O. Jones, Proc. Phys. Soc. London 89, 443 (1966).

[8]J. B. Pendry and F. Forstmann, J. Phys. C. 3, 59 (1970).

[9]F. Forstmann and V. Heine, Phys. Rev. Lett. 24, 1419 (1970).

[10]J. N. Schulman and T. C. McGill, Solid State Commun. 34, 29 (1980); Phys. Rev. B (in press).

[11]G. C. Osbourn and D. L. Smith, Phys. Rev. B 19, 2124 (1979).

[12]H. P. Hjalmarson, P. Vogl, D. J. Wolford, and J. D. Dow, Phys. Rev. Lett. 44, 810 (1980).

[13]H. P. Hjalmarson, Ph.D. thesis, University of Illinois at Urbana-Champaign, 1979 (unpublished).

[14]H. P. Hjalmarson, P. Vogl, and J. D. Dow, J. Phys. Chem. Solids (in press).

[15]D. J. Chadi and M. L. Cohen, Phys. Status Solidi B 68, 405 (1975).

[16]See, for example, M. Abramowitz and I. A. Stegun, *Handbook of Mathematical Functions* (Dover, New York, 1970), p. 17.

[17]See, for example, O. Madelung, *Introduction to Solid-State Theory* (Springer, New York, 1978), p. 59.

[18]E. I. Blount, in *Solid State Physics,* edited by F. Seitz and D. Turnbull (Academic, New York, 1962), Vol. 13, p. 305.

[19]C. Herring, Phys. Rev. 32, 365 (1937).

[20]These special features are due to that the conduction band for ZnTe obtained in the current tight-binding model does not have a maximum for k_z in the middle of the Brillouin zone, whereas the conduction band obtained from a pseudopotential calculation (Ref. 21) does. Since a complex band will emanate from the local maximum of this band and connect up a higher band, we expect these special features for ZnTe will disappear in the pseudopotential calculation.

[21]M. L. Cohen and T. K. Bergstresser, Phys. Rev. 141, 789 (1966).

[22]Ed Caruthers, L. Kleinman, and G. P. Alldredge, Phys. Rev. B 9, 3301 (1974).

[23]L. Kleinman, Phys. Rev. B 11, 3900 (1975); 12, 2547 (1975).

[24]R. E. Allen, Phys. Rev. B 19, 917 (1979).

[25]R. E. Allen, Phys. Rev. B 20, 1454 (1979).